# Autonomous Robotic Drilling System for Mice Cranial Window Creation

Enduo Zhao, Murilo M. Marinho, Senior Member, IEEE, and Kanako Harada, Member, IEEE

Abstract—Robotic assistance for experimental manipulation in the life sciences is expected to enable favorable outcomes, regardless of the skill of the scientist. Experimental specimens in the life sciences are subject to individual variability and hence require intricate algorithms for successful autonomous robotic control. As a use case, we are studying the cranial window creation in mice. This operation requires the removal of an 8-mm circular patch of the skull, which is approximately 300  $\mu$ m thick, but the shape and thickness of the mouse skull significantly varies depending on the strain of the mouse, sex, and age. In this work, we develop an autonomous robotic drilling system with no offline planning, consisting of a trajectory planner with execution-time feedback with drilling completion level recognition based on image and force information. In the experiments, we first evaluate the image-and-force-based drilling completion level recognition by comparing it with other state-ofthe-art deep learning image processing methods and conduct an ablation study in eggshell drilling to evaluate the impact of each module on system performance. Finally, the system performance is further evaluated in postmortem mice, achieving a success rate of 70% (14/20 trials) with an average drilling time of 9.3 min.

Note to Practitioners-This paper addresses the challenge of drilling over a trajectory with specified depth using image and force information. The proposed strategy compensates at execution time for unknown characteristics such as shape, thickness, and operational noise which are common to organic matter such as eggs and mice skulls. The trajectory is general but for this work, it is evaluated as circular. Pre-operatively, sufficient training data (e.g., videos) must be obtained and manually annotated with the pixel-wise completion level. At the training stage, this annotation for completion can be discretized into classes (e.g., 0%, 25%, 50%, 75%, 100%) to facilitate annotation. These annotations are utilized to train the entire multimodal model, including image and force, therefore no additional force annotation is needed. This single data gathering generalizes over individual differences because the visual features that correlate with pixel-wise completion are not dependent on the overall shape and size of the surface. We apply this strategy to many fragile targets with individual variations such as raw chicken eggs and postmortem mice skulls. Nonetheless, a success rate of 100% has not yet been achieved because even human annotators struggle to differentiate completion levels in mice skulls. The inclusion of other sensorial modalities might be needed for further progress.

This work was supported by JST Moonshot R&D JPMJMS2033. (*Corresponding author:* Murilo M. Marinho)

Enduo Zhao was with the Department of Mechanical Engineering, Graduate School of Engineering, The University of Tokyo, Tokyo, Japan, when this work was conducted. He is currently with the School of Biomedical Engineering, Tsinghua University, Beijing, China. Email:endowzhao@mail.tsinghua.edu.cn.

Murilo M. Marinho is a visiting researcher with the Graduate School of Medicine, the University of Tokyo, Tokyo, Japan. He is also with the Department of Electrical and Electronic Engineering, the University of Manchester, Manchester, UK. He has been supported by the Robotics and AI Collaboration (RAICo). Email:murilo.marinho@manchester.ac.uk.

Kanako Harada is with the Center for Disease Biology and Integrative Medicine, Graduate School of Medicine, The University of Tokyo, Tokyo, Japan. Email:kanakoharada@g.ecc.u-tokyo.ac.jp.

Index Terms—Multi-Arm Robotic Platform, Cranial Window Creation, Multi-sensor Fusion.

#### I. INTRODUCTION

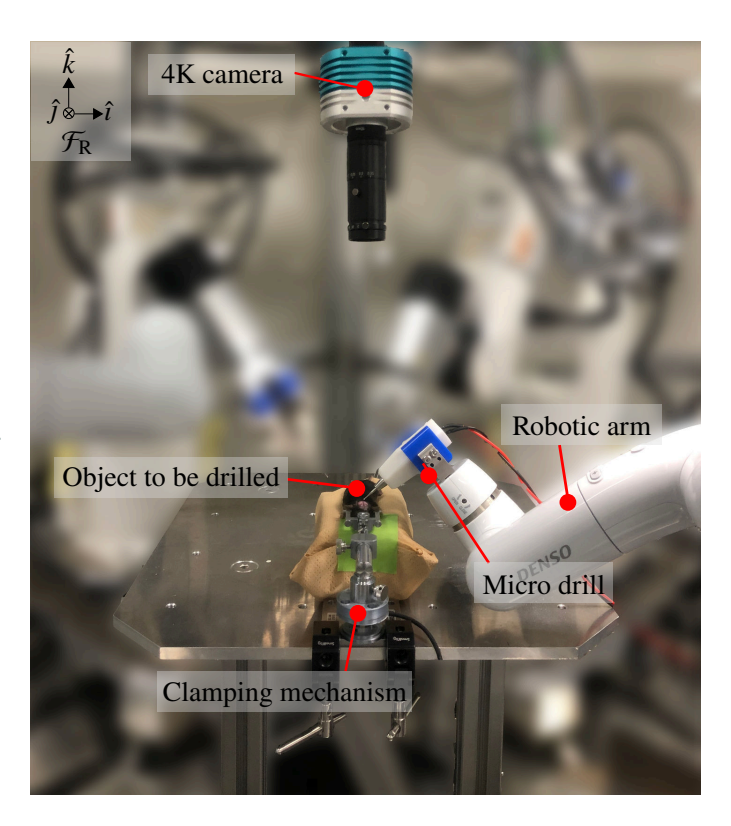


Fig. 1. The system setup used in this work consists of one of the 8-degrees-of-freedom robotic branches of an AI-robot platform for scientific exploration [1]. For this work, we attached a micro drill as an end effector. In addition, we use a 4K camera and a clamping mechanism for the object being drilled.

cranial window is a transparent observation window carefully created in the skull of a mouse, providing direct visualization and access to the brain for experimental purposes. For example, a cranial window can be utilized to observe human organoids that are implanted into the mouse brain [2]. Cranial window creation involves using a micro drill under a microscope to extract an 8-mm circular patch of the mouse skull, which is then replaced with a cover glass [3], [4]. This technique is crucial for advancing our understanding of human cell growth and developing strategies for diagnosing, treating, and preventing neurological disorders. However, variabilities in surface flatness, skull thickness and density complicate the operation, and the small size and delicate nature of mouse skulls increase the risk of damaging critical structures during the procedure [3], [5], [6], leading to inflammation, infection,

bleeding, or even the death of the mouse. This constitutes a catastrophic failure, as it prevents the subsequent implantation and observation of human cells [3], [7]. These factors further compound the complexity and difficulty of the experiment.

In many biological procedures analogous to cranial window creation, robotic systems equipped with multimodal sensing and real-time control play a significant role by adaptively performing complex tasks amid anatomical variability. For instance, Liu et al. [8] developed an electromagnetic system achieving sub-40 µm trajectory precision in intraocular microsurgery through disturbance-rejection control and thermaloptimized actuation, while Wang et al. [9] developed a multimodal sensor-enabled soft robotic system that achieves 100% recognition accuracy even for geometrically identical objects through feature-level sensor fusion and adaptive grasping control. Building upon such advancements, robotic systems are increasingly regarded as promising solutions to overcome many of the challenges associated with cranial window creation in mice, by performing repetitive tasks with higher precision, reducing the task time, and enhancing the quality of the experiments. Numerous devices and robotic systems have been devised to aid in cranial window creation. Pohl et al. [10] designed a robotic module for assisting mouse craniotomy by monitoring force and sound signals, estimating drilling penetration, and controlling drill feed speed. However, further automating cranial window creation using a robotic system presents greater challenges in terms of the robot's perceptual and adaptive capabilities. This is mainly due to the uncertainties in both the external and internal characteristics of the mouse skull, such as uneven surfaces, non-uniform thickness, fragile membrane beneath the skull, and potential deformations occurring during drilling. Therefore, the system needs to be able to obtain and process not only global information, for global planning of the drilling trajectory, but also contact signals, for real-time feedback to handle dynamic changes. Our team is investigating scientific experiments' automation using a robotic manipulator retrofitted with a micro drill, as shown in Fig. 1, with cranial window creation being one of the intended automation targets.

As an end goal, cranial window creation must be conducted on anesthetized mice given the nature of the experiments. However, relying on live mice for studying autonomous robot control in relatively early stages of research raises ethical concerns. Therefore, initially we rely on training procedures used for human technical specialists [11] and surgical trainees [12], which comprises removing a circular patch of chicken eggshell without damaging the underlying membrane.

In previous research [13], an autonomous robotic drilling system was developed and preliminarily validated in autonomously drilling eggshells using image feedback. In this study, by incorporating force feedback and a plane-fitting algorithm, we report improved efficacy and speed in eggshell drilling. With these sizable improvements over the state-of-the-art, in this work, we show the first-in-the-World example of effective mouse drilling without pre-processing on *postmortem* mice, which is a large step towards the automation of the cranial window creation in live mice. Note that no mice were

euthanized in this research<sup>1</sup>.

Although we showcase the work in a scientific exploration background, our system can be seen as a multimodal adaptive autonomous robotic drilling system. The system can generalize to unknown surface and thickness of the drilled object without additional data thanks to the trajectory planner and the exteroceptive drilling completion level recognition.

### A. Related works

Some studies have partially addressed the challenges of automating cranial window creation using robotic systems. Pak *et al.* [14] demonstrated a penetration detection strategy using a measurement circuit that detects electrical conductance between the drill and the mouse, indicating skull penetration by a sudden increase in conductance. Hasegawa *et al.* [17] proposed a drilling system that judges the local penetration by extracting feature values based on force and sound signals, achieving automatic drilling and being evaluated on the egg model. These studies based on the perception of contact signals such as force, sound, and electrical signals can only make judgments about whether penetration occurs at the local position in contact with the drill bit, as the perception signals are generated only during contact. This will result in a lack of global awareness of the entire drilling trajectory.

To perceive global information, Ghanbari et al. [15] developed a cranial microsurgery platform "Craniobot" that employs a surface profiler and micro-computed tomography to assess skull surface topology and thickness. These data are utilized to create a 3D drilling path towards the desired depth. Jeong et al. [16] utilized the metrology via second harmonic generation to map mouse skull surfaces and establish a drilling path, then employed plasma-mediated laser ablation for drilling purposes. Navabi et al. [19] combined optical coherence tomography (OCT) and machine learning to obtain the skull anatomy, which was then used for trajectory planning and automated drilling. These works are capable of the perception of global information, but obtaining the pre-operative information of every mouse would be time-consuming due to the individual differences, and over-reliance on pre-operative information may result in the system's inadequate executiontime feedback on dynamic changes in the characteristics of the skull during drilling as well as unexpected situations. Additionally, the research by Jeong et al. [16] and Navabi et al. [19] introduced advanced sensors with high cost, which makes the methods impractical to implement broadly.

Our previous work [13] developed an autonomous robotic drilling system for mice cranial window creation with only image-based completion level recognition as the perception on global information and preliminarily proved its feasibility by eggshell drilling experiment. However, the lack of local contact signals still results in some limitations in lag in updating recognized penetration of occlusion areas by drill and a lack of sufficient accuracy, particularly for pixels with drilling

<sup>1</sup>The *postmortem* mice used in this work were donated to us after an unrelated and ethically approved experimentation in a neighboring research laboratory. The mice would have otherwise been discarded. Hence, no additional ethical committee approval was sought for the purposes of this work.

TABLE I CAPABILITIES OF THE PROPOSED WORK IN CONTRAST WITH EXISTING LITERATURE.

	This work	[13]	[14]	[15]	[16]	[17]	[18]	[19]
Contact signals <sup>1</sup>	√	×			×			×
Global information <sup>2</sup>	√					×		
No pre-operative information			×	×	×	×		×
No accurate simulation required <sup>3</sup>							×	
No use of specialized sensors <sup>4</sup>			×		×			×
Execution-time feedback			×	×				×
Validated on mice		×				×	×	
Assessment metrics available <sup>5</sup>			Δ	Δ	Δ	Δ	×	Δ

<sup>&</sup>lt;sup>1</sup>Sensors are used for contact detection/estimation include force sensor, audio, and electrical conductance.

completion levels higher than 0.8. Jia et al. [18] presented a 3-phase periodic Bayesian reinforcement learning method for the eggshell drilling task as a simulation of cranial window creation and achieved successfully drilling and automatically acquiring spatial information about the eggshell terrain via the information of 2D image, force, and audio signal instead of 3D scanning in advance. This work combined the processing of contact signals and global awareness along the trajectory and does not require any pre-operative information input. Regrettably, the work was evaluated on an egg model rather than on mice, and the Bayesian reinforcement learning needs a dedicated simulator for training, reducing its practicality.

In summary, the aforementioned studies either focus on local penetration detection or rely on pre-operative information, with few effectively combining the two, which limits their real-time adaptability to skull variations. Some of these works employ specialized sensors or simulations, affecting their broad practicality. It is also worth noting that except for [13], the related studies did not consistently report experimental metrics of drilling speed or success rate, which makes it difficult for direct comparison. Considering the limitations of previous studies, we aim to propose an autonomous robotic drilling system for mice cranial window creation that can perceive both contact signals and global information without pre-processing, specialized sensors, or simulators. To achieve this, our system primarily relies on image processing using a neural network for perception, while force signals serve as auxiliary inputs. Additionally, we conduct repeat experiments and evaluate the results with general metrics. The contrast of the capabilities of the proposed work with existing literature is shown in Table I.

### B. Statement of contributions

In this work, we show a trajectory planner and a multimodal recognition method with image and force information, capable of perceiving global information and contact signals, enabling fully autonomous operation in *postmortem* mice, in addition to 7.1 min average drilling (136% faster) with increased (95% vs. 80%) success rate in autonomous eggshell drilling. In detail, we propose (1) a trajectory planner based on constrained

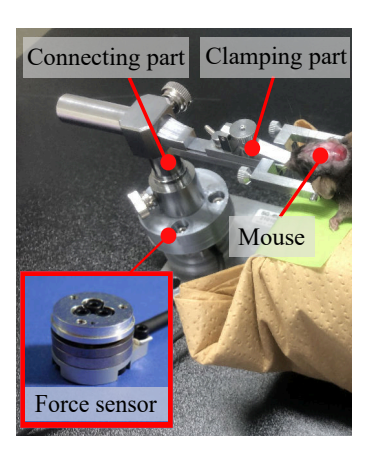


Fig. 2. The clamping mechanism for mouse skulls including a commercial mouse skull holder and a force sensor.

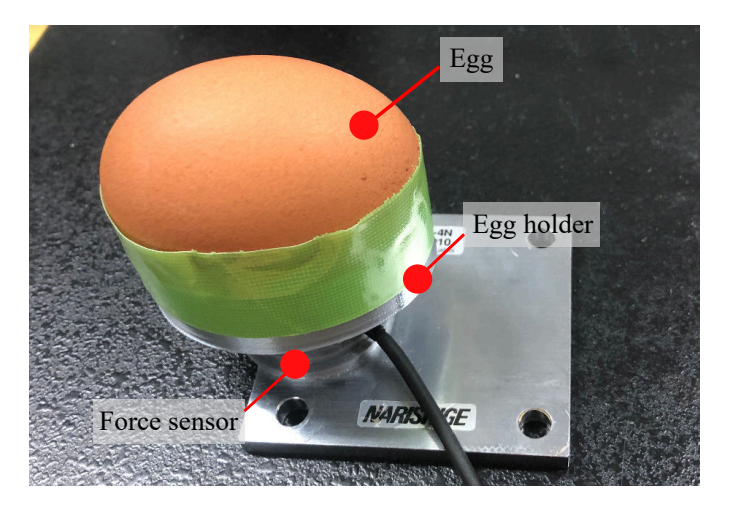


Fig. 3. The clamping mechanism for eggs including a 3D printed holder and a force sensor.

splines and execution-time plane fitting that is adjusted in realtime by image and force feedback, (2) a drilling completion level recognition module based on deep neural networks with multi-branch architectures to update the planned trajectory at execution-time with image and force information. The force

<sup>&</sup>lt;sup>2</sup>Sensors are used to collect global information on the entire surface. These include a camera, force sensors to measure points in the surface, micro-CT scanner, OCT, and ultrashort pulsed Ti-sapphire oscillator.

<sup>&</sup>lt;sup>3</sup>An accurate computer simulation was part of the workflow. This means that it would not be applicable to mice given the complexities of simulating mice's skin, bones, and other structures.

<sup>&</sup>lt;sup>4</sup>Specialized sensors were included in the system. This means the work is more difficult to reproduce and implement broadly.

<sup>&</sup>lt;sup>5</sup>Repeat experiments were conducted and general metrics (success rate, average operation time) are available to assess the performance of the system.  $\Delta$  refers to when only success rate or speed was evaluated.

information increases the resolution of recognition 10 times and provides information on drilled areas under occlusion. In addition, we evaluate (3) the performance of the drilling completion level recognition integrating image and force information, (4) the impact of new modules via ablation study in fully autonomous robotic drilling experiments using eggshells, and (5) present the first-in-the-World fully autonomous results of cranial window drilling in *postmortem* mice.

### II. PROBLEM STATEMENT

Consider the setup shown in Fig. 1, using one of the robotic arms of our robot platform for scientific exploration [1]. Let R be the 8-degrees-of-freedom serial manipulator with joint values  $q \in \mathbb{R}^8$  composed of the robotic arm (CVR038, Densowave, Japan), linear actuator, and circular rail actuator. Let R be holding the micro drill (MD1200, Braintree Scientific, USA) that is used to drill the object (i.e. either the eggshell or the mouse skull) fixed by our clamping mechanism. The clamping mechanism contains a force sensor (ThinNANO, BL AUTOTEC, Japan). For mice, the clamping part is a head holder (SG-4N, NARISHIGE, Japan), shown in Fig. 2. And for eggs it is a custom-designed 3D printed egg holder. The force sensor has a custom-designed 3D printed casing to fix the force sensor underneath the egg holder, shown in Fig. 3. Images are obtained from above through a 4K microscope system (STC-HD853HDMI, Omron-Sentech, Japan) equipped with a distortionless macro lens of f = 75 mm (VS-LDA75, VS Technology, Japan), set vertically above the center of the mouse or egg to observe the drilling procedure. Only for the system of eggshell drilling, an air compressor (Model OF301-4B, Jun-Air, USA) with a silicone tube is applied to blow away the shell dust emitted from drilling the surface of the eggshell.

### A. Goal

Our goal is to autonomously drill the object (eggshell or mouse skull) along a circular path with respect to the base frame of the robot system,  $\mathcal{F}_R$  (see Fig. 1), without requiring target-specific data collection, pre-training with accurate simulation, pre-processing, or surface measurement. In addition to proprioceptive information (kinematics and encoders), the goal is to use accessible sensors (camera and force sensor) to gather information for execution-time feedback, including global information, primarily for monitoring the drilling process, as well as contact signals to support predictions in occluded regions. The method can achieve an effect similar to a dynamically changing visual virtual fixture, without any pre-settings.

# B. Overview of the proposed system

The overview of the proposed system is shown in Fig. 4. In our strategy, the robotic system block interacts with the object (eggshell or mouse skull) while global information and contact signals of the drilling procedure are acquired by sensors (4K camera and force sensor) assembled in the multimodal robotic system. The information is processed and converted into a

generic dynamic parameter, the drilling completion level c, by the drilling completion level recognition block (introduced in Section III). c is an n-dimensional vector in which each element  $\mathbb{R} \ni c_i \triangleq c_i \, (t) \in [0,1]$  stands for the completion percentage of drilling at the i-th measure point along the trajectory, where  $c_i = 0$  means not drilled and  $c_i = 1$  means completely drilled. The drilling completion level-based trajectory planner (introduced in Section IV) updates the continuous trajectory at execution time. The robot's tooltip trajectory is calculated by the constrained inverse kinematics algorithm [1], which outputs joint commands to the robotic system, closing the loop.

#### III. DRILLING COMPLETION LEVEL RECOGNITION

The drilling completion level recognition block consists of three parts: namely, image-based completion level recognition (Section III-A), force-based completion level recognition (Section III-B) and completion level results integration (Section III-C). The image-based and force-based completion level recognition parts can independently recognize the drilling completion levels ( $c_{\rm image}$  and  $c_{\rm force}$ ) for selected measure points on the trajectory, and the two results are integrated into c for improved performance and higher resolution.

# A. Image-based completion level recognition

For image-based completion level recognition, we propose a single network to jointly detect the drilling area and estimate the drilling completion level, leveraging the synergistic benefits known from co-training complementary task such as detection and semantic segmentation [20]. The algorithm and network remain unchanged from the previous study [13], whose architecture is inspired by DSSD [21] and contains two branches for bounding-box detection and completion level estimation. The main improvement is that in this paper, a mouse skull dataset is built and applied to retrain the network in preparation for mouse skull drilling experiments. More training details (network architecture, hyperparameter tuning, evaluation of joint training, and training condition) are available in the supplementary material.

- 1) Training dataset creation: The datasets were specifically generated for this task. In our former study [13], we collected 518 images from videos of teleoperated robotic eggshell drilling experiments performed by our group on 12 eggs that comprised the eggshell dataset and expanded it to 16,576 images after augmentation methods of random flip, rotate, random crop, and random change of brightness and contrast. In order to apply the network to the mouse skull, we collected 587 images from videos of teleoperated mouse skull drilling experiments performed by our group on 10 postmortem mice for the mouse skull dataset (18,784 after augmentation). Both datasets were annotated manually and split 80 %-10 %-10 % for training, validation, and testing.
- a) Data annotation: Generally, ground truth images with full manual annotation are required for multi-task learning. In this work, we expect our network to output a bounding box of the drilling area and a completion level map. When generating

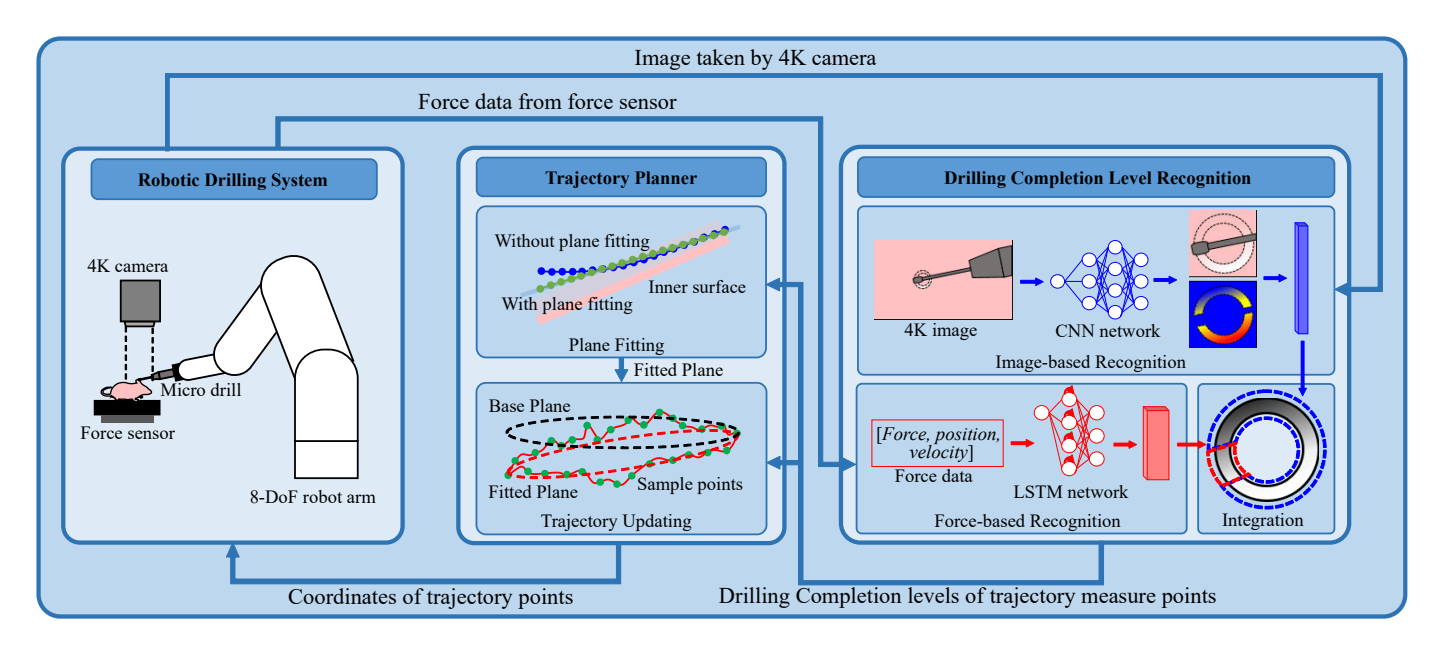


Fig. 4. Block diagram of the proposed autonomous robotic drilling system.

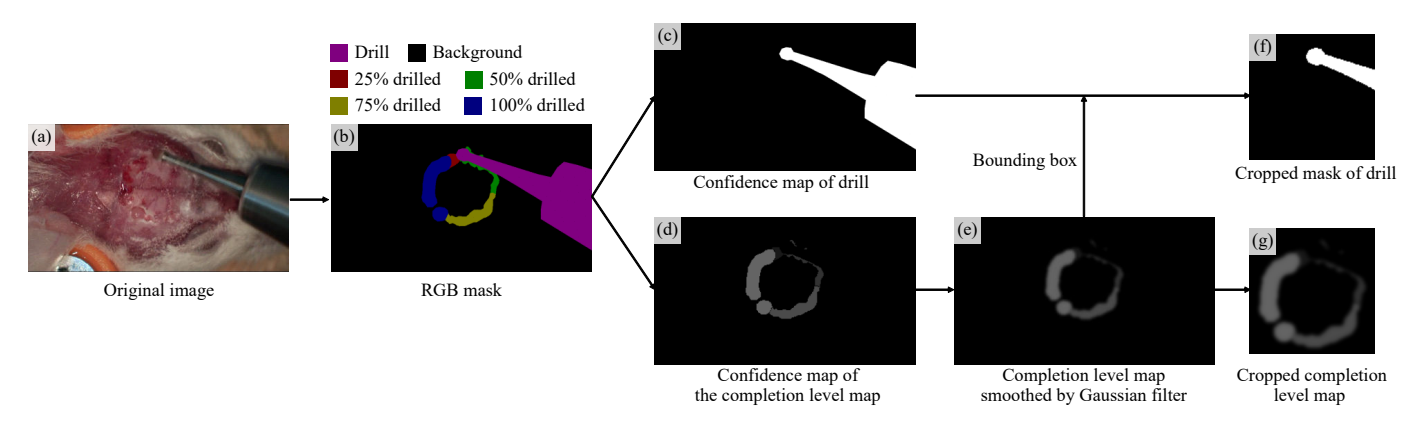


Fig. 5. An example of creating the training dataset. (a) An original image of mouse skull drilling. (b) RGB mask that is labeled manually in 6 classes: Drill, 0% drilled (Background), 25% drilled, 50% drilled, 75% drilled, and 100% drilled. (c) Confidence map of the drill. (d) Confidence map of the completion level map. (e) The completion level map is smoothed by a Gaussian filter. (f) Cropped drill mask within the drilling region. (g) Cropped completion level map within the drilling region.

the ground truth of completion level maps, manually annotating each pixel with a grayscale value ranging from 0 to 100 is not feasible (0 of grayscale refers to the completion level of that pixel c=0 while 100 refers to c=1). We propose a more treatable annotation strategy.

To describe the annotation procedure, let us use a mouse skull drilling image, but the process is the same for eggshell images. As shown in Fig. 5-(a), given an image, first we define 6 classes for a semantic segmentation classifier: drill, 0% drilled (background), 25% drilled, 50% drilled, 75% drilled, and 100% drilled as shown in Fig. 5-(b). The percentage of drilling completion is defined subjectively based on the video with our experience in pilot studies. Second, at a higher level in the hierarchy, we separate the image into two confidence maps. The first one is for pixels of the drill, as shown in Fig. 5-(c), with 255 corresponding to the full confidence, so that the drill can be removed from the mask. The second confidence map corresponds to the completion level map, as shown in Fig. 5-(d), where 0 of grayscale corresponds to 0% drilled

pixels and 100 corresponds to 100% drilled pixels. Lastly, taking advantage of the expected continuity in drilled regions, a Gaussian filter is applied to smooth the completion level map channel so that its grayscale values of pixels are continuous from 0 to 100, as shown in Fig. 5-(e).

The bounding box is automatically annotated. A 4-dimensional vector  $(x_1, y_1, x_2, y_2)$  is used as the ground truth of the bounding box detection branch, which is generated from the completion level map channel by noting the minimum value and maximum value from width and height direction of those pixels whose grayscale values are not 0. After that, we crop both the completion level map channel and drill channel using the coordinate of the bounding box  $(x_1, y_1)$  and  $(x_2, y_2)$  and then resize them into  $128 \times 128$ , satisfying the requirement of real-time processing. Merging two channels together we can get a  $128 \times 128 \times 2$  matrix as the ground truth of the completion level estimation branch, as shown in Fig. 5-(f)(g).

2) Training result and evaluation: The output results of an eggshell image and a mouse skull image are shown in Fig. 6.

The bounding box detection and cropped image show the output from the network for the detected drilling area and the cropped result of the area. The heatmap of completion shows a visualization of the drilling completion levels recognition result of parts that are drilled and not occluded by the drill, while untouched or occluded parts are suppressed.

mAP (mean Average Precision) is applied as the evaluation metric for object detection while MAPE (Mean Absolute Percentage Error) is applied as the evaluation metric of completion level estimation task. Our model is able to reach up 78.5 in mAP for detection and 15.05 % in MAPE for estimation while the frequency is 72 for the eggshell dataset. For the mouse skull dataset, the speed is unchanged, the mAP for detection is 77.6, and the MAPE for estimation is 24.32 %. Based on the experiment results in our former research [13], reasonable values in this application are mAP > 75, MAPE < 25 % and real-time (FPS > 60), so our work is able to achieve a good trade-off.

We also obtain a progress bar of the drilling procedure by normalizing the corresponding pixel value. The progress bar is generated by not only the completion level map in this moment but also those in the past because we expect the drilling progress of an area to be monotonically increasing. By setting m discrete points evenly along the circle on the progress bar, we obtain a  $c_{\text{image}}$  with size of m and elements  $c_{i,\text{image}} \in [0,1] \subset \mathbb{R}$ , namely the image-based drilling completion level at any point i, where  $i=1,\cdots,m\in\mathbb{N}$ . The value of m is 32 considering the resolution of the image.

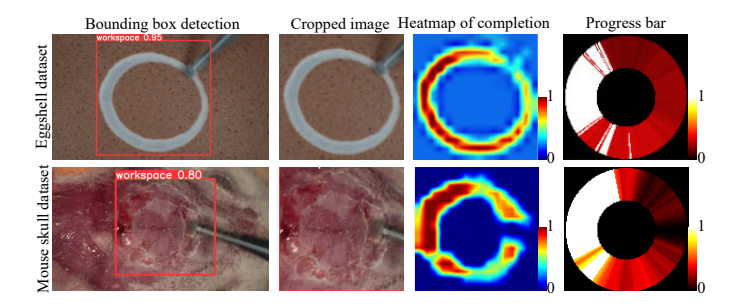


Fig. 6. Output results from the network. The original image with the bounding box, the cropped image, the heatmap, and the progress bar of the completion level map are outputs for post-processing and visualization. Color bars are attached to the heatmap and the progress bar, which will be omitted in subsequent images.

### B. Force-based completion level recognition

The force-based completion level recognition is an addition over our previous research [13]. In order to compensate for the inaccuracy of image processing in estimating results when the drilling completion level is higher than 0.8, to address the occlusion of points by the drill, and to increase spatial resolution, we added a force-based Long Short-Term Memory Recurrent Neural Network (LSTM-RNN) [22]. This approach takes advantage of the higher spatial accuracy of the force information (w.r.t. image information) and the significant difference in stiffness between the membrane and the skull or eggshell. We utilize force data collected during the drilling

procedure to predict the drilling completion level at the current and subsequent drilling regions.

We posit that recognizing the drilling completion levels in the vicinity of the drill-surface contact area can be achieved by analyzing the measurement values of the force sensor and the position and velocity state of the drill over a short history (e.g., the past few seconds). To implement this recognition, we employ an LSTM-RNN whose structure is inspired by [23]. More training details (network architecture and training conditions) are available in the supplementary material.

1) Training dataset: The proposed LSTM-RNN takes force, positions, and velocities of the drill in past l seconds as the input, and outputs the drilling completion levels from time t to t+k in the future as the drill moves a complete circular trajectory on the x-y plane. Note that t denotes the current moment, and k is the predictable number of future time. Assuming that the sampling frequency of the force sensor is f, the sample size of the input data is L=fl, and the sample size of output data is K=fk. Considering our drilling speed of 16 seconds per turn, we chose l=16 and k=4 considering the size of the occlusion area. The sampling frequency of the force sensor was set as f=20 Hz. Thus the sample sizes of input data and output data are L=320 and K=80, respectively.

To train the model, we conducted 10 autonomous (imageonly) drilling trials each on eggshells and mice, recording force  $F_x, F_y, F_z$ , position x, y, z, descent speed  $v_z$ , and drilling completion level c. The ground truth for c was obtained through the manual annotation (see Fig. 5) and upsampled to 320 points to match the sensor data resolution.

Each trial produced an  $S \times 8$  matrix (S being the total samples), which was cut into S-L-K sets of size  $L \times 7$  (input) and  $K \times 1$  (output) for training. The eggshell dataset contained 84,000 samples (80,000 sets after cutting), and the mouse skull dataset had 87,600 samples (83,600 sets after cutting). Both datasets were split 80%-10%-10% for training, validation, and testing.

2) Training result and evaluation: The LSTM-RNN is expected to output the prediction result of drilling completion levels from time t to t+k, so we can expect that predicted drilling completion level at time  $t+\Delta t$  ( $0\leqslant \Delta t\leqslant k$ ) should be an implicit variable in  $\Delta t$ . By comparing the prediction result at time  $t+\Delta t$  with the ground truth, the prediction accuracy of the network for  $\Delta t$  time forward can be calculated, denoted as acc ( $\Delta t$ ). In our case, we allow a difference between predicted and true value within 0.05.

The curves of changes in accuracy  $acc\left(\Delta t\right)$  for the eggshell dataset and the mouse skull dataset are illustrated as the red and blue lines in Fig. 7-(a). When  $\Delta t=0$ , the accuracies of both curves reach their maximum value,  $88.60\,\%$  for the eggshell dataset and  $77.43\,\%$  for the mouse skull dataset. As  $\Delta t$  increases, both curves show a decreasing trend. For the eggshell dataset, the lowest accuracy  $52.61\,\%$  occurs when  $\Delta t=3.45$ , while for the mouse skull dataset, the lowest accuracy  $41.21\,\%$  is at  $\Delta t=3.50$ . The result is in line with our predictions because larger  $\Delta t$  is farther into the future, which is more difficult for the neural network to predict. By

linear fitting of the accuracy using the least squares method, we can obtain an expression for the accuracy

$$acc(\Delta t) = a \cdot \Delta t + b(\%). \tag{1}$$

For the eggshell dataset, the values of parameters a and b are a=-7.94, b=81.43. For the mouse skull dataset, the parameter values are a=-7.07 and b=74.01. The variation in accuracy influences the integration strategy, which will be discussed in Section III-C. Additionally, an example of the forces landscape and the prediction completion level result when  $\Delta t=0$  is shown in Fig. 7-(b).

The output of the LSTM-RNN  $c_{\text{force}}$  is a vector with size K=80 and each element value  $c_{i,\text{force}} \in [0,1] \subset \mathbb{R}$  refers to the drilling completion level at at a future moment t+i/f in terms of temporal span.

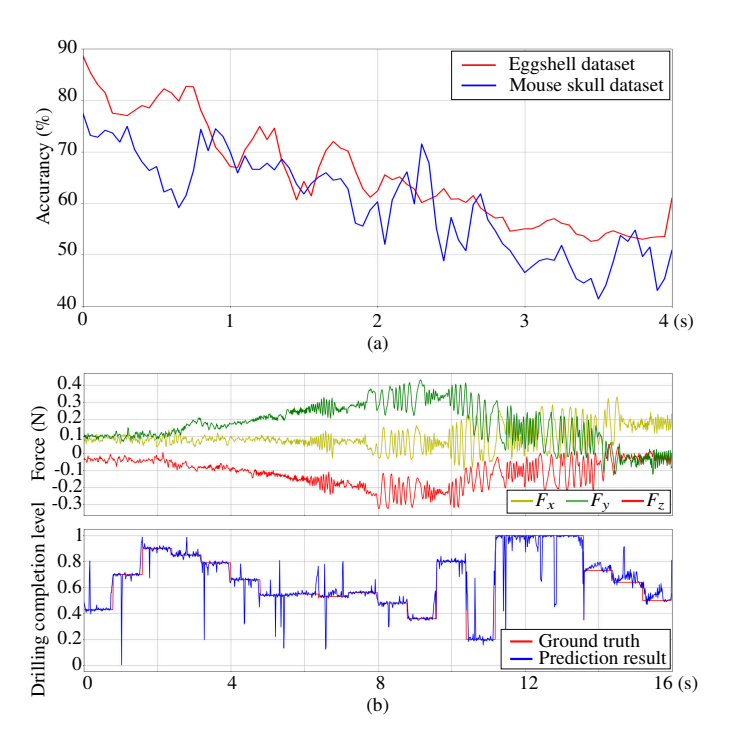


Fig. 7. Training results of the LSTM-RNN. (a) The image of the change in accuracies of completion level recognition  $acc\left(\Delta t\right)$  with  $\Delta t$  for eggshell dataset (red line) and mouse skull dataset (blue line) based on data from time t-l to t; (b) Forces landscape and the prediction result at time t within a drilling turn.

### C. Completion level results integration

In Section III-A and Section III-B, the drilling completion levels were independently recognized based on image and force information, albeit at different spatial and temporal scales. The advantage of image-based recognition is that the image taken by the upper camera provides single-shot drilling completion levels of all points along the trajectory, while the disadvantages are relatively low spatial resolution and occlusion issues. On the other hand, force-based recognition can predict the instantaneous changes in drilling completion levels of the contact area at the current moment with high accuracy and resolution without occlusion issues but has little global prediction power besides a close future. In order to

make good use of the advantages of both recognition methods, in this work we propose an integration strategy.

1) Synchronization: Our system uses ROS Noetic Ninjemys for data acquisition, distribution, and communication, including advanced message synchronization to align timestamps between 4K camera images and force sensor data, addressing temporal inconsistencies in sensor fusion [24]. However, harmonizing the differing lengths and sample rates from sensors remains necessary.

The image-based completion level output,  $c_{\rm image}$ , has m=32 measure points (described in Section III-A), while the force-based output,  $c_{\rm force}$ , has K=80 points (described in Section III-B). By padding  $c_{\rm force}$  with zeros and upsampling  $c_{\rm image}$ , we expand the size of both vectors to n=320. This ensures that both vectors have the same size, with each element corresponding to the drilling completion level at the same trajectory point based on image and force data. More details on synchronization are available in the supplementary material.

2) Data fusion: As mentioned in Section II-B, our ultimate goal is to obtain the drilling completion level c with size of n, generated by the fusion of image and force. The completion level c can be calculated as

$$c = w_1 \odot c_{\text{image}} + w_2 \odot c_{\text{force}}, \tag{2}$$

where  $\odot$  denotes the element-wise product of two vectors, and  $w_1$  and  $w_2$  are the weight vectors with size of n whose elements are the weight of the corresponding element in  $c_{\text{image}}$  and  $c_{\text{force}}$ .

The force-based accuracy weights,  $w_2$ , are derived using the accuracy function  $acc_i = a \cdot \Delta t_i + b\,(\%)$ , where  $\Delta t_i = i/f$ ,  $i=1,\cdots,K\in\mathbb{N}$ , and f is the force sensor frequency. The parameters a and b are set as -7.94, 81.43 for eggshells and -7.07, 74.01 for mouse skulls (discussed in Section III-B). Similar to  $c_{\text{force}}$ , we also fill  $w_2$  with extra elements of zeros, expanding its size to n=320. Whenever there is occlusion, the image-related results are less reliable, therefore we set  $w_1=1-w_2$ . Substituting the results of  $w_1$  and  $w_2$  into (2), the integration result c can be calculated.

Compared with our previous research [13], with the integration of force information, the accuracy of the completion level recognition improves close to the current drilling area and the spatial resolution of the completion level recognition increases 10 fold. The recognition result of the multimodal integration is used in (3).

# IV. DRILLING COMPLETION LEVEL-BASED TRAJECTORY PLANNER

In the last section, the drilling completion level recognition block outputs the integration result of the completion level c that is a discrete set of n values (n=32 for [13] using only image and n=320 for the proposed image and force module). Nonetheless, the robot must be given a continuous trajectory for smooth performance using our inverse kinematics calculation [1]. In this section, we present a trajectory planner that generates a continuous trajectory for autonomous drilling, where each point on the trajectory has a fixed coordinate value

in the x-y plane while the z-axis coordinate is updated based on the drilling completion level.

In formal terms, let the desired drill path be discretized into n equal intervals resulting in the points  $p_i(c_i) \triangleq \left[p_{x,i} \quad p_{y,i} \quad p_{z,i}\left(c_i\right)\right]^{\mathrm{T}} \in \mathbb{R}^3, \ i=1,\cdots,n\in\mathbb{N},$  defined with respect to the base frame of the robotic manipulator  $\mathcal{F}_{\mathrm{R}}$  (see Fig. 1).  $c_i$  is the drilling completion level of each point i recognized from the image and force, detailed in Section III. The goal of the trajectory planner is to obtain a continuous trajectory that is circular when projected in the x-y plane and causes all n drill points to be complete in finite time by updating the z-axis position,  $p_{z,i}$ , using the drilling completion level  $c_i$ . We hypothesize that, by using a proper interpolation methodology, if all n points (the ones we can effectively measure online) are sufficiently drilled, then the entire trajectory (including the points that we cannot directly measure) will be sufficiently drilled.

The proposed trajectory planner is divided into three steps. First, imbued with each drilling completion level (obtained in Section III),  $c_i$ , we calculate each  $p_{z,i}\left(c_i\right)$  as discussed in Section IV-A. Second, a plane is fitted based on those points  $p_i\left(c_i\right)$  whose drilling completion level  $c_i\neq 0$ , obtaining an offset  $o_{z,i}$  between each point and its projection on the plane to update  $p_{z,i}\left(c_i\right)$  on the trajectory as discussed in Section IV-C. Lastly, with the z-axis coordinate for each of the n measure points defined in the previous step and given the desired trajectory topology, we obtain the continuous drill path using a constrained spline interpolator as discussed in Section IV-B.

### A. z-axis trajectory calculation: multimodal velocity damper

The core of our automatic drilling proposal is to reduce the downward velocity  $v_{z,i} \triangleq v_{z,i} (c_i) \in \mathbb{R}$  of a given trajectory point i proportionally to its drilling completion level  $0 \leqslant c_i \leqslant 1$ , obtained via multimodal information as shown in Section III. The velocity is modulated as follows

$$v_{z,i}(c_i) = (1 - c_i) v_z.$$
 (3)

This means that when a trajectory point i has drilling completion level  $c_i=0$ , it is untouched, hence  $v_{z,i}\left(0\right)=v_z$  and the robot moves at nominal velocity  $v_z$  downward, where  $v_z$  is a design parameter with a negative value (e.g., -1 mm/s), since the upward direction is defined as the positive direction in the base frame of the robot system  $\mathcal{F}_R$ . When the trajectory point has  $c_i=1$ , that point has been fully drilled and the downward velocity becomes  $v_{z,i}\left(1\right)=0$ , meaning that the robot will not drill further. Intermediate levels of completion allow the system to behave smoothly with respect to the drilling completion level.

Although effective, a direct implementation of (3) has been shown in our previous work [13] to be inefficient when the target circular drill surface is not aligned with the robot's x-y plane.

In this work, we augment (3) with an online estimation of the target x-y drill plane using  $c_i$ , described in Section IV-C. Considering the simple integration of (3) with a sampling time T, the plane-fitted position-based algorithm becomes

$$p_{z,i}(t+T) = p_{z,i}(t) + v_{z,i}(c_i)T + o_{z,i}(t),$$
(4)

where  $o_{z,i}(t)$  is the plane-fitted offset, detailed in Section IV-C. This way, the drilling traverses through empty space much faster by estimating the surface plane of the target and adapting accordingly.

# B. Continuous trajectory generation: constrained cubic spline interpolation

Since the z-axis coordinate for each of the n measure discrete points  $p_{z,i}\left(c_i\right)$  has been updated in the previous section, the purpose of this section is to generate a continuous drilling path based on these points to match the high precision encoders used in the robotic system. Cubic spline interpolation has been widely applied for generating continuous paths from discrete points but it is, by itself, unsuitable for our application as it might overshoot between two trajectory measure points and cause rupture to the membrane (see Fig. 8). Instead, we propose the use of constrained spline interpolation by eliminating the requirement for equal second order derivatives at every point and replacing it with specified first order derivatives [25]. As an improvement over our previous work [13], we focus on the relevant coordinates given that our trajectory is cylindrical.

Let the trajectory points be  $\begin{bmatrix} p_{x,i} & p_{y,i} & p_{z,i} \end{bmatrix}^T$ ,  $i = 1, \dots, n \in \mathbb{N}$ . We express them under a cylindrical coordinate system  $\begin{bmatrix} p_{\rho,i} & p_{\varphi,i} & p_{z,i} \end{bmatrix}^T$ . The z-axis coordinate  $p_{z,i}$  is the same for both expressions while

$$p_{\rho,i} \triangleq \sqrt{p_{x,i}^2 + p_{y,i}^2} = \frac{d}{2} ,$$
 $p_{\varphi,i} = \operatorname{atan2}(p_{y,i}, p_{x,i}) ,$ 
(5)

where d is the diameter of the cylinder, which is a constant value of 8 mm in our setup and the function  $\operatorname{atan2}(y,x)$  calculates the polar angle of the point  $(x,y) \neq (0,0)$  taking values in  $(-\pi,\pi]$ . As a result, interpolation happens in  $\mathbb{R}^2$ , namely the points  $\boldsymbol{\rho}_i = \left[\begin{array}{cc} p_{\varphi,i} & p_{z,i} \end{array}\right]^{\mathrm{T}}$  with  $p_{\varphi,i} \in [-\pi,\pi) \subset \mathbb{R}$  and  $p_{z,i} \in \mathbb{R}$ .

Let  $\varphi$  be the independent variable to generate a curve  $s(\varphi) = \begin{bmatrix} \varphi & s_z(\varphi) \end{bmatrix}^T$  through  $[-\pi,\pi)$ . We have then a set of piecewise curves  $s_i(\varphi) = \begin{bmatrix} \varphi & s_{z,i}(\varphi) \end{bmatrix}^T$ , each *i*-th curve describing a curve between two contiguous points  $\rho_i$  and  $\rho_{i+1}$ . By the definition of a cubic spline, each curve is a third-degree polynomial given by

$$s_{z,i}(\varphi) \triangleq a_{z,i} + b_{z,i}\varphi + c_{z,i}\varphi^2 + d_{z,i}\varphi^3, \tag{6}$$

whose first-order derivative of (6) is

$$\dot{s}_{z,i}(\varphi) \triangleq b_{z,i} + 2c_{z,i}\varphi + 3d_{z,i}\varphi^2. \tag{7}$$

In order to calculate the parameters of the curve, we need three continuity conditions. First, given that the domain for each  $s_i\left(\varphi\right)$  is  $\left[p_{\varphi,i},p_{\varphi,i+1}\right]$ , each piecewise curve must pass through its "left" endpoint  $p_i$  and "right" endpoint  $p_{i+1}=\left[\begin{array}{cc}p_{\varphi,i+1}&p_{z,i+1}\end{array}\right]^{\mathrm{T}}$ , that is,

$$s_{z,i}\left(p_{\omega,i}\right) \triangleq p_{z,i},\tag{8}$$

$$s_{z,i} \left( p_{\varphi,i+1} \right) \triangleq p_{z,i+1}. \tag{9}$$

Second, the first-order derivative of the whole curve must be continuous, which means the whole curve is continuously differentiable at each  $p_i$ . Its first-order derivative,  $\dot{p}_{z,i}$ , is a free parameter. In traditional cubic spline interpolation, the third condition is to define the second-order derivative for each measure point as  $\ddot{p}_{z,i}$ . As a result, the generated trajectory is smooth enough but overshoot might occur.

For constrained cubic spline interpolation, instead, we aim to solve the overshoot problem by sacrificing smoothness. We constrain the first-order derivative to prevent overshoot between two contiguous points as

$$\dot{s}_{z,i}\left(p_{\varphi,i}\right) \triangleq \dot{p}_{z,i},\tag{10}$$

$$\dot{s}_{z,i}\left(p_{\varphi,i+1}\right) \triangleq \dot{p}_{z,i+1},\tag{11}$$

where the intention is to ensure that the first order derivative at a point will be between the slope of the two adjacent lines joining that point, and should approach zero if the slope of either line approaches zero. Furthermore, the first order derivative of a point should be 0 if the signs of the slope of the two lines are different from each other to define this point as a local minimum to prevent overshoot. To define a first order derivative that satisfies the conditions, we denote the product of the differences between the z-coordinates of a point  $p_{z,i}$  and its left point  $p_{z,i-1}$  and right points  $p_{z,i+1}$  as

$$t_i \triangleq (p_{z,i+1} - p_{z,i}) (p_{z,i} - p_{z,i-1}),$$
 (12)

so the first order derivative at the point can be calculated as

$$\dot{p}_{z,i} \triangleq \begin{cases} \frac{2}{\frac{p_{\varphi,i+1}-p_{\varphi,i}}{p_{z,i+1}-p_{z,i}} + \frac{p_{\varphi,i}-p_{\varphi,i-1}}{p_{z,i}-p_{z,i-1}}} & \text{if } t_i > 0\\ 0 & \text{otherwise} \end{cases} . (13)$$

It is important to note that (12) and (13) are only valid when  $2 \leqslant i \leqslant n-1$ . Considering the projection of the curve on the x-y plane is a circle, the first point and the end point of the trajectory are adjacent. We can define  $t_1 \triangleq (p_{z,2}-p_{z,1})(p_{z,1}-p_{z,n})$  and  $t_n \triangleq (p_{z,1}-p_{z,n})(p_{z,n}-p_{z,n-1})$ . So when  $t_1 > 0$  or  $t_n > 0$ , (13) can be adjusted to obtain

$$\dot{s}_{z}(p_{\varphi,1}) = \dot{p}_{z,1} \triangleq \frac{2}{\frac{p_{\varphi,2} - p_{\varphi,1}}{p_{z,2} - p_{z,1}} + \frac{p_{\varphi,1} - (p_{\varphi,n} - 2\pi)}{p_{z,1} - p_{z,n}}},$$
(14)

$$\dot{s}_{z}\left(p_{\varphi,n}\right) = \dot{p}_{z,n} \triangleq \frac{2}{\frac{(p_{\varphi,1} + 2\pi) - p_{\varphi,n}}{p_{1} - p_{z,n}} + \frac{p_{\varphi,n} - p_{\varphi,n-1}}{p_{z,n} - p_{z,n-1}}}.$$
 (15)

We can calculate all coefficients by combining (6), (7), (8), (9), (10), and (11) into

$$\begin{bmatrix} a_{z,i} \\ b_{z,i} \\ c_{z,i} \\ d_{z,i} \end{bmatrix} = \begin{bmatrix} 1 & p_{\varphi,i} & p_{\varphi,i}^2 & p_{\varphi,i}^3 \\ 1 & p_{\varphi,i+1} & p_{\varphi,i+1}^2 & p_{\varphi,i+1}^3 \\ 0 & 1 & 2p_{\varphi,i} & 3p_{\varphi,i}^2 \\ 0 & 1 & 2p_{\varphi,i+1} & 3p_{\varphi,i+1}^2 \end{bmatrix}^{-1} \begin{bmatrix} p_{z,i} & p_{z,i+1}^2 & p_{z,i+1}^2$$

By substituting (13), (14), and (15) into the right side of (16), we can get the value of coefficients expression  $a_{z,i}$ ,  $b_{z,i}$ ,  $c_{z,i}$ , and  $d_{z,i}$ . We can obtain the expression of any piecewise third-degree polynomial curves  $s_i(\varphi)$  and, consequently, know the entire curve  $s(\varphi)$ . The cylindrical coordinates are mapped back into the Cartesian space  $\mathcal{F}_R$  by the reverse coordinate transformations of (5) before going into the manipulator's inverse kinematics calculation [1]. Fig. 8

shows a qualitative comparison between a traditional cubic spline interpolation and its constrained version. This is to show that the green curve is enveloped by the tangent planes but red the curve is not, hence illustrating the problem of overshoot.

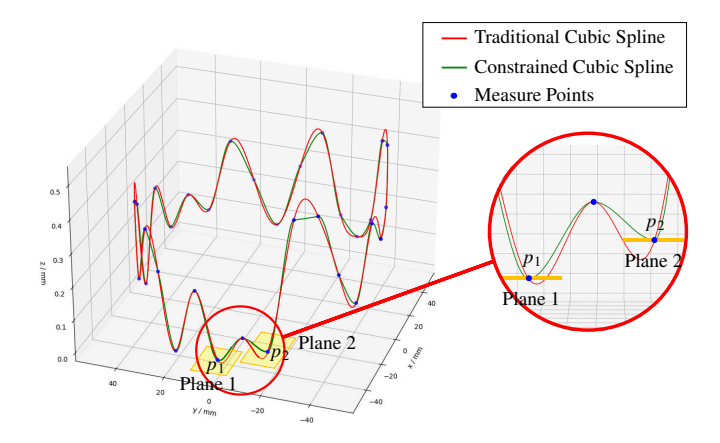


Fig. 8. Generated curve based on a certain amount of measure points along the circular path. The blue points are the measure points, the red line is the result of traditional spline interpolation, and the green line is the result of constrained spline interpolation. We can see the red line overshoots while the green does not.

### C. Plane fitting

As mentioned in the previous work [13], the problem of the long drilling time and potential failure cases were partially caused by a tilted initial pose. In this work, we address this issue with an execution-time plane fitting, which is to find the least squares plane of the measure points whose drilling completion levels are not 0 (given that they are the only points about which we have enough information) to accelerate the drilling procedure.

After the plane fitting, the original points on the trajectory should be updated to the fitted plane. At time t, consider a certain point on the trajectory  $\boldsymbol{p}_i(t) \triangleq \begin{bmatrix} p_{x,i}(t) & p_{y,i}(t) & p_{z,i}(t) \end{bmatrix}^{\mathrm{T}}$ , the z coordinate of the corresponding point on the fitted plane is denoted as  $p'_{z,i}(t)$  and the offset  $o_{z,i}(t)$  in (4) can be calculated by

$$o_{z,i}(t) = p'_{z,i}(t) - p_{z,i}(t)$$
.

We tested the trajectory planner with plane fitting on part of the trajectory points in simulation and found that the trajectory adapted to the surface faster by 43% with plane fitting, which is in line with our expectation. More details on the mathematical description and simulation testing of the plane fitting are available in the supplementary material.

# V. EXPERIMENTS

Comparing with our previous system that recognized the drilling completion level solely based on image [13], in this study, the force-based completion level recognition and the plane fitting were introduced. To evaluate the drilling completion level recognition integrated with force signals, we compare it with the state-of-the-art deep learning image processing methods. Then, to verify the impact of the two new modules

TABLE II
THE COMPARISON RESULTS OF THE PROPOSED METHOD WITH OTHER STATE-OF-THE-ART DEEP LEARNING IMAGE PROCESSING MODELS.

Network	MAPE (%) on egg				MAPE (%) on mice				FPS	
Network	Original	Low blur	Medium blur	High blur	Original	Low blur	Medium blur	High blur	113	
CABiNet [26]	14.25	18.95	23.28	31.87	25.52	28.03	28.80	51.14	77	
BiSeNet (Res18) [27]	15.20	19.20	23.21	31.89	25.61	27.78	28.85	50.35	66	
PP-LiteSeg-T2 [28]	14.42	19.00	22.76	30.81	24.01	27.53	30.20	49.35	96	
PP-LiteSeg-B2 [28]	13.97	18.85	22.35	30.66	23.87	27.23	29.65	47.92	67	
SFNet (DF2) [29]	12.95	18.23	22.01	30.45	22.96	27.35	30.05	46.43	88	
DDRNet-23-S [30]	12.78	17.92	21.11	30.29	22.62	27.01	29.15	45.01	108	
PIDNet-S-Simple [31]	12.38	17.78	20.58	30.27	21.54	26.98	28.31	45.25	101	
PIDNet-S [31]	12.25	17.65	20.43	30.12	21.32	26.64	27.70	44.93	93	
Image only [ours]	14.97	19.23	22.95	31.03	23.92	27.70	29.97	51.05	73	
Image + Force [ours]	9.47	13.31	14.47	27.89	20.38	24.45	25.36	40.94	68	

on improving the system performance, we conducted ablation studies on eggshell drilling. Lastly, we use the whole system to conduct an experiment on *postmortem* mouse skull drilling to validate its effectiveness. A video of the experiments is shown in the supplementary material and available at https://youtu.be/e1ZEtLM033Y.

### A. Hardware setup & preparation

The hardware of the system is set up as described in Section II and shown in Fig. 1. As for the image-based and force-based completion level recognition models, the eggshell drilling experiment uses the pre-trained model on the eggshell dataset, while the mouse skull drilling experiment uses the pre-trained model on the mouse skull dataset. Before the experiment starts, the micro drill is teleoperated by an operator to adjust the starting point so that it is within the field-of-view of the camera throughout the entire circular path.

#### B. Software implementation

The experiments use a software implementation on a Ubuntu 20.04 x64 system. The robotic arm is controlled as described in [1]. ROS Noetic Ninjemys is used for the interprocess communication and CoppeliaSim (Coppelia Robotics, Switzerland) for the simulations. Communication with the robot is enabled by the SmartArmStack<sup>2</sup>. The dual quaternion algebra and robot kinematics are implemented using DQ Robotics [32] with Python3. The force sensor is connected to a Raspberry Pi 4 Model B and the force data is read at 128 samples per second (SPS) using Python's SMBus module and an I2C analog input board. More details about the software implementation are available in the supplementary material.

### C. Parameters selection

The parameters used in the experiments, namely the initial speed  $v_z$  of the drill in (3), the diameter of the circular drilling path d, and the frequency f of the transmission of the calculated z-positions to the robot are selected to be  $v_z \triangleq -6 \times 10^{-6}$  m/s based on a comparative experiment (detailed in the supplementary materials),  $d \triangleq 8$  mm based on the demand for follow-up experiments and the size of mice, and  $f \triangleq 30$  Hz based on the requirement of high precision

encoders used in the robotic system. The drilling will stop autonomously when the system judged the drilling completion criterion is met. This happens when 80% of the points on the drilling path achieve at least 0.85 of completion level, consistent with the literature [13].

# D. Experiment 1: evaluation of the drilling completion level recognition

Our proposed drilling completion level recognition method is based on the image-based element and the force-based element, evaluated in Section III-A2 and Section III-B2, respectively. Therefore, in this experiment, we evaluate the complete method and compare it to other state-of-the-art realtime semantic segmentation models. Note that considering that the target tasks are different, the output of other semantic segmentation models are adjusted to be two channels: the completion level map channel and drill channel, the same as those of our method. Moreover, our proposed imagebased completion level recognition can perform bounding box detection and completion level estimation simultaneously but other models can only estimate the drilling completion level. For a fair comparison, we crop the images manually for the compared works to focus on the drilling area and resize it into  $128 \times 128$  (the same as the output size of our completion level estimation branch) to serve as the input for the evaluation of other models, while the original whole image is applied directly for our model.

- 1) Evaluation dataset: Three autonomous drilling trials on egg and one on mouse are conducted for evaluation, with 4K images obtained from the camera and force signals obtained from the force sensor. These data are for evaluation only and are not included in the training dataset. Additionally, in order to evaluate the robustness of the models, we apply Gaussian filters with kernel sizes k=3, k=5, and k=7 to the images, adding low, medium, and higher blur, respectively.
- 2) Metrics: Same as Section III-A2, MAPE is the accuracy metric and FPS is recorded to evaluate the computation speed.
- 3) Results and discussion: The comparison results are summarized in Table II. Noting that we require the drilling completion level recognition to provide a real-time feedback, so only the result of models with FPS > 60 are shown. We can conclude from the result that with the integration of force signals, our method of drilling completion level recognition

<sup>&</sup>lt;sup>2</sup>https://github.com/SmartArmStack

has the best performance and robustness in MAPE while satisfying the requirement of real-time.

# E. Experiment 2: ablation study of the new modules on eggshell

To evaluate the impact of the two new modules on system performance: the force-based completion level recognition and the plane fitting, we design and implement an ablation study using eggshell drilling experiments to quantify the contribution of each module by comparing system performance under different combinations of modules.

- 1) Ablation setting: Settings for ablation study are summarized in Table III, where the other three groups are to integrate the force-based completion level recognition module or the plane fitting module into the baseline, as well as to integrate both modules.
- 2) Metrics: For each setting, 20 trials are conducted using eggs of random shape, size, and shell thickness. The drilling procedure ends when the drilling completion criterion is met (see Section V-C) or manually stopped if significant membrane damage is observed. Performance is evaluated via success rate and average drilling time for successful cases, with additional failure mode metrics to quantify risks:
  - Success rate: Percentage of trials where the resected eggshell piece can be manually removed without membrane damage, an example shown in Fig. 9-(a). Failure occurs if the result is under-drill or over-drill (modelinduced or human-intervened).
  - Under-drill rate: Percentage of trials where the drilling completion criterion is met, but the eggshell is not manually removable, an example shown in Fig. 9-(b).
  - Model-induced over-drill rate: Percentage of trials where the drilling completion criterion is met, but the membrane has been ruptured, an example shown in Fig. 9-(c).
  - Human-intervened over-drill rate: Percentage of trials
    where the for drilling completion criterion is NOT met,
    but significant membrane damage is observed and the
    experiment is compulsory stopped manually, an example
    shown in Fig. 9-(d). The human-intervened over-drill case
    is the most dangerous case, which could potentially lead
    to the death of mice in future experiments with live mice.
  - Average drilling time: Time from drill initiation to autonomous stop, calculated only for successful trials.

These metrics collectively capture trade-offs between precision, speed, and autonomy, indicating safer and more reliable performance.

3) Results and discussion: Results of all settings are shown in Table III, and the success rates and average drilling time are illustrated in Fig. 10.

Compared to the Baseline, integrating the force-based completion level recognition improved the success rate (90 % vs. 80 %) and reduced the average drilling time (14.7 min vs. 16.8 min) in eggshells. The introduction of force data allowed information to be updated when the drilled region was occluded, preventing human-intervened over-drilling (0 % vs. 10 %), which is the failure mode we least want to occur. This reduction also results from the high resolution of force

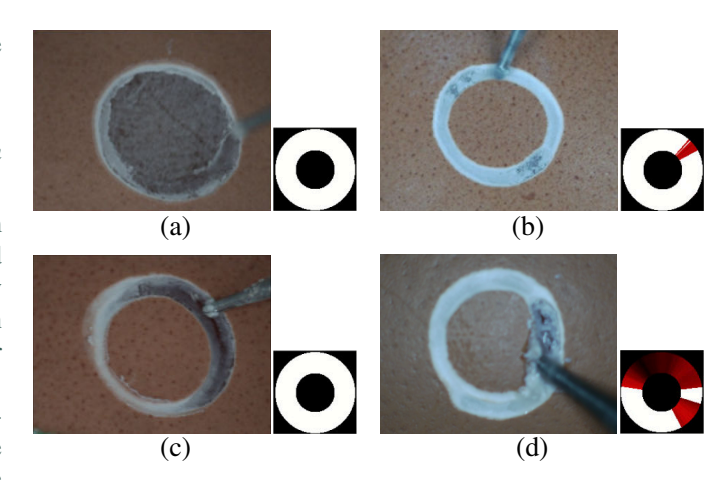


Fig. 9. Example result images and corresponding progress bars of (a) a successful case; (b) a failure case of under-drill; (c) a failure case of model-induced over-drill; and (d) a failure case of human-intervened over-drill.

signal, which resolves ambiguities in drilling completion level recognition solely based on images and allows more accurate recognition when near penetration. However,  $5\,\%$  modelinduced over-drilling persisted due to long drilling time, where the drill bit ruptures the membrane surface despite retaining its z-position at points reaching a drilling completion level of 1 when the drill is trying to drill the other points that are not. Despite this, the total over-drilling risk decreased from  $15\,\%$  to  $5\,\%$ , demonstrating the benefit of force-based completion level recognition.

Integrating the plane fitting significantly improved the drilling speed (8.0 min vs. 16.8 min) and slightly improved the success rate (85 % vs. 80 %) in eggshells, compared to the Baseline. This suggests that the long drilling time and failures caused by varying egg initial poses in our former research were overcome by the plane fitting. However, the accelerated drilling speed occasionally exceeds the system's ability to dynamically update drilling completion levels, leading to a higher rate of human-intervened over-drill (15 % vs. 10 %) and increasing risks.

Integration of the two new modules achieved the highest success rate (95%) and fastest drilling (7.1 min), while eliminating all over-drilling risks (0 % model-induced and 0 % human-intervened over-drill). Noting that the only failure was caused by under-drill, meaning that the drilling completion criterion was met so the drilling stopped automatically, but the eggshell inside the drilling area could not be removed by tweezers manually. This suggests that in future work the drilling completion criterion needs to be adjusted. For example, an iterative learning system could be implemented to refine the threshold that is currently constant. Alternatively, a non-rotating drill bit could be controlled to automatically press the eggshell within the drilling area and observe its displacement to determine whether it is detachable, mimicking the same inspection procedure performed by human operators in practical mice cranial window creation. Additionally, a ttest was conducted to evaluate the differences in performance between the integration groups and the Baseline and the pvalues are shown in Fig. 10, demonstrating that integrating

TABLE III
SETTINGS FOR ABLATION STUDY AND THE RESULTS.

Ablation setting	Success (%)	Under drill (%)	Over-	-drill (%)	- Average drilling time (min)	
		Under-drill (%)	Model-induced	Human-intervened		
Image only (Baseline)	80	5	5	10	16.8	
Image + Force	90	5	5	0	14.7	
Image + Plane fitting	85	0	0	15	8.0	
Full	95	5	0	0	7.1	

either of the new modules, or both of the modules can lead to statistically significant improvements in system performance.

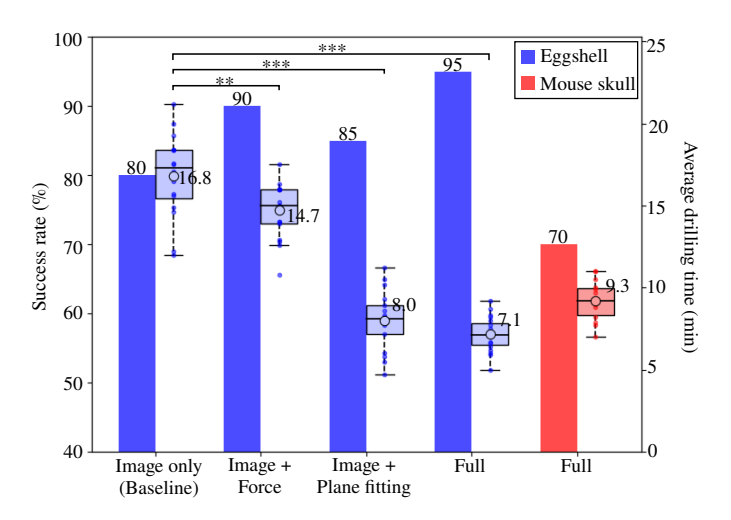


Fig. 10. Comparison of the results for all settings on eggshells (described in Table III), as well as the result of mouse skull. The bar chart represents the success rate with different settings while the box plot represents the average drilling time.

# F. Experiment 3: validation experiment on postmortem mouse skull

In Experiment 2, we showed that with the integration of new modules the autonomous robotic drilling system performed well on eggshells, however, it is still necessary to verify the feasibility on mouse skull drilling. 20 trials on 20 different *postmortem* mice are conducted. Similar to the eggshell experiment, the resected circular mouse skull patch being removable manually with tweezers defines successes and failures.

Results and discussion: In the experiment, 14 out of 20 cases were successful, resulting in a success rate of 70%. The average required time for successful drilling was 9.3 min. The result of postmortem mouse skull drilling is also shown in Fig. 10, with a representative successful case illustrated in Fig. 11. In the case, the drilling procedure stopped automatically when it was judged as complete and the circular patch was removed perfectly. We can conclude that the system effective for mouse skull drilling with a considerable success rate and drilling speed.

Five of the six failure cases were human-intervened overdrill because of incorrect completion level recognition, and the remaining one was under-drill. Compared with the results of eggshell drilling, the completion level recognition is considered less accurate for mouse skulls due to more complex images and textures. For image-based recognition, the color changes in mouse skulls are subtler and influenced by factors like individual variation, skull humidity, and the time between euthanasia and the experiment. For example, moist skulls shortly after euthanasia show minimal color change during drilling, while drier skulls appear whiter as drilling progresses. These variations complicate recognition. Force-based recognition is also affected by skull moistness, which alters stiffness, and by fluid exudation during drilling. Bleeding in some trials changed both stiffness and color, further reducing accuracy. Additionally, reflected light from wet skull surfaces negatively impacts recognition. Applying more data augmentation methods to the mouse skull dataset (e.g., random bleeding, random light reflection), generating photo-realistic synthetic data in a more complex environment, and adding random noise to the force training dataset could be potential future work to further enhance the robustness of our system.

#### G. Conclusion and discussion

The results of the evaluation experiments with different settings (described in Table III) on eggshell and mouse skulls are shown in Fig. 10, which demonstrate the effectiveness and robustness of our autonomous robotic drilling system. More complex models of neural network for both image-based and force-based recognition, which are more robust to changes in the color or moistness change, can help to some extent but processing speed can suffer. Additional sources of information, such as audio or vibration, can be added in future work to improve robustness.

We compared our results with those of other related studies on creating a cranial window of similar size ( $d=8\,\mathrm{mm}$ ), as shown in Table IV. Note that most works did not conduct repeat experiments to evaluate their system with a success rate and only provided a vague drilling time, which results in the difficulties in compare the robustness and speed. We are the only research to evaluate the system with a general metrics to demonstrate the performance.

### VI. CONCLUSION

In this paper, we propose an autonomous robotic drilling system for mice cranial window creation. To achieve this, a trajectory planner that can adapt to the drilled object and prevent overshoot is imposed, and a plane fitting method is added to solve the problem caused by long drilling time. In order to adjust the generated trajectory in real-time, we apply neural networks to recognize the drilling completion level based on image and force data obtained during the drilling procedure. In the experiments, we show that the proposed

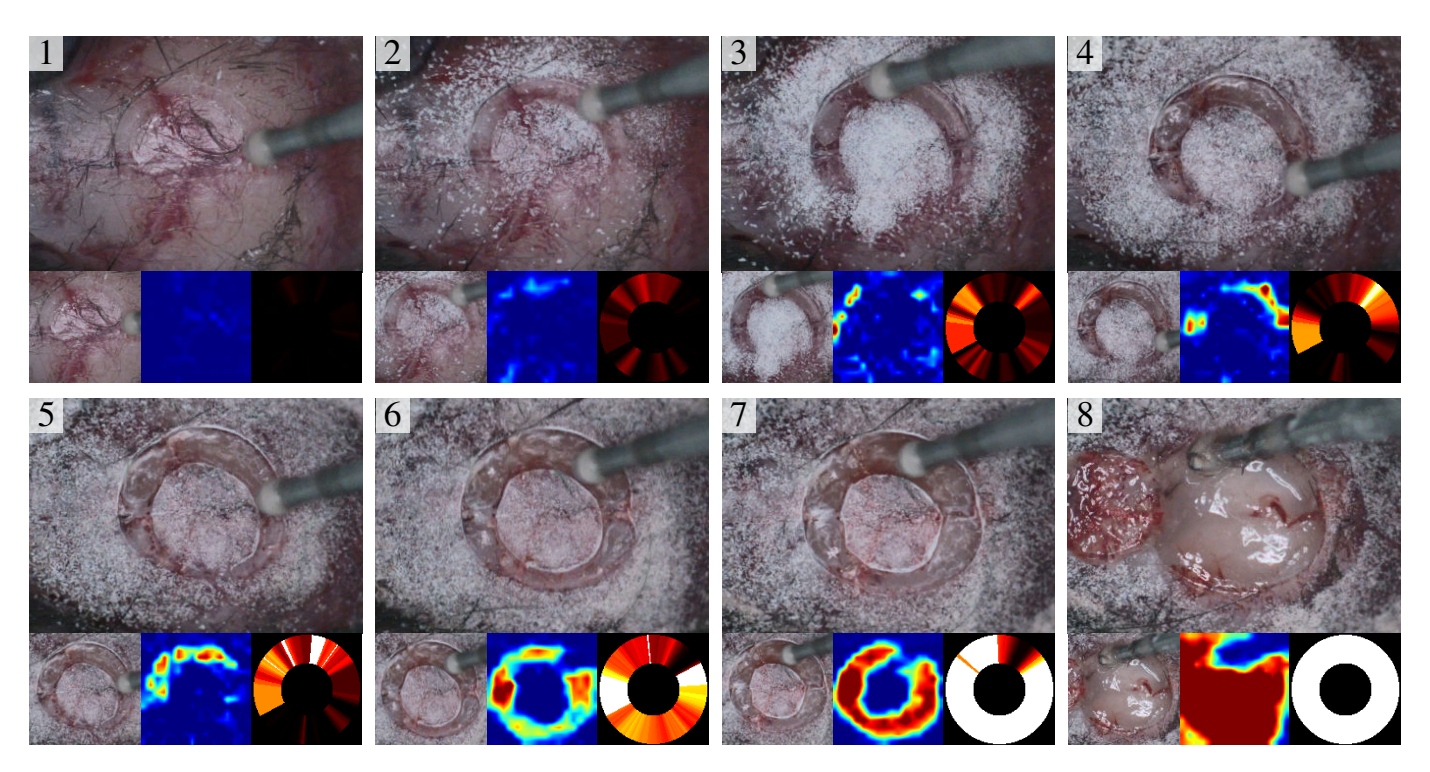


Fig. 11. A series of snapshots of a case of successful drilling on a *postmortem* mouse skull from the start of drilling to the removal of resected circular shell piece. Original image, cropped image, heatmap (generated by image processing), and drilling progress bar (generated based on the estimation result of both image and force) are shown for each snapshot.

TABLE IV
COMPARISON OF THE PROPOSED WORK IN CONTRAST WITH EXISTING LITERATURE.

Object	Metrics	This work	[13]	[14]	[15]	[16]	[17]	[18]	[19]
Faa	Success rate (%)	95 (n = 20)	$80 \ (n=20)$	N.A.	N.A.	N.A.	$100 \ (n=2)$	N.A.	N.A.
Egg	Average time (min)	7.1	16.8	N.A.	N.A.	N.A.	N.A.	N.A.	N.A.
Mice	Success rate (%)	$70 \ (n=20)$	N.A.	N.A.	N.A.	N.A.	N.A.	N.A.	N.A.
IVIICE	Average time (min)	9.3	N.A.	$< 15 \ (n = 15)$	10-15 $(n=6)$	N.A.	N.A.	N.A.	< 5 (n = 2)

system is able to achieve a considerable success rate and speed in autonomous eggshell drilling and demonstrate the possibility of the system on autonomous mice cranial window creation.

Different from existing studies, which either focus on local penetration detection, rely on pre-operative global information, or employ specialized sensors or simulations, our system integrates perceived contact signals and global information to successfully achieve a real-time, adaptive, and generalizable drilling trajectory generation and planning method without pre-processing. Additionally, we provide experimental metrics, including drilling speed and success rate, establishing a standard for comparing related studies.

Our ultimate goal is the autonomous cranial window creation on anesthetized live mice which require the mice to be alive and remain alive after the procedure. This is a considerable challenge in aspects that are being investigated in parallel to this work, such as surgical conditions, anesthesia, sterilization, ethical board approval, and other aspects. In this work we present a clear step towards this goal. To further approach this ultimate goal, future work will include enhancing the robustness of the completion level recognition block by fine-tuning the neural network, adopting a more accurate and

objective drilling completion criterion, and improving the success rate of drilling by incorporating additional modalities such as audio. Furthermore, given that many surgeries, including orthognathic surgery and arthroplasty, face similar challenges related to target uncertainty in surface and thickness, we aim to extend the application of our autonomous robotic drilling system to other medical fields.

# REFERENCES

- M. M. Marinho, J. J. Quiroz-Omaña, and K. Harada, "A multiarm robotic platform for scientific exploration: Its design, digital twins, and validation," *IEEE Robotics & Automation Magazine*, pp. 2–12, 2024.
- [2] H. Koike, K. Iwasawa, R. Ouchi, M. Maezawa, K. Giesbrecht, N. Saiki, A. Ferguson, M. Kimura, W. L. Thompson, J. M. Wells, A. M. Zorn, and T. Takebe, "Modelling human hepato-biliary-pancreatic organogenesis from the foregut-midgut boundary," *Nature*, vol. 574, no. 7776, pp. 112–116, sep 2019.
- [3] A. Holtmaat, T. Bonhoeffer, D. K. Chow, J. Chuckowree, V. De Paola, S. B. Hofer, M. HÃŒbener, T. Keck, G. Knott, W.-C. A. Lee, R. Mostany, T. D. Mrsic-Flogel, E. Nedivi, C. Portera-Cailliau, K. Svoboda, J. T. Trachtenberg, and L. Wilbrecht, "Long-term, high-resolution imaging in the mouse neocortex through a chronic cranial window," *Nature Protocols*, vol. 4, no. 8, pp. 1128–1144, Jul. 2009.
- [4] G. J. Goldey, D. K. Roumis, L. L. Glickfeld, A. M. Kerlin, R. C. Reid, V. Bonin, D. P. Schafer, and M. L. Andermann, "Removable cranial windows for long-term imaging in awake mice," *Nature Protocols*, vol. 9, no. 11, pp. 2515–2538, Oct. 2014.

- [5] P. J. Drew, A. Y. Shih, J. D. Driscoll, P. M. Knutsen, P. Blinder, D. Davalos, K. Akassoglou, P. S. Tsai, and D. Kleinfeld, "Chronic optical access through a polished and reinforced thinned skull," *Nature Methods*, vol. 7, no. 12, pp. 981–984, Oct. 2010.
- [6] G. Yang and W. Gan, "Sleep contributes to dendritic spine formation and elimination in the developing mouse somatosensory cortex," *Developmental Neurobiology*, vol. 72, no. 11, pp. 1391–1398, Jul. 2012.
- [7] T. H. Kim, Y. Zhang, J. Lecoq, J. C. Jung, J. Li, H. Zeng, C. M. Niell, and M. J. Schnitzer, "Long-term optical access to an estimated one million neurons in the live mouse cortex," *Cell Reports*, vol. 17, no. 12, pp. 3385–3394, Dec. 2016.
- [8] Y. Liu, D. Song, G. Zhang, Q. Bu, Y. Dong, C. Hu, and C. Shi, "A novel electromagnetic driving system for 5-dof manipulation in intraocular microsurgery," *Cyborg and Bionic Systems*, vol. 5, p. 0083, 2024. [Online]. Available: https://spj.science.org/doi/abs/10.34133/cbsystems. 0083
- [9] T. Wang, T. Jin, W. Lin, Y. Lin, H. Liu, T. Yue, Y. Tian, L. Li, Q. Zhang, and C. Lee, "Multimodal sensors enabled autonomous soft robotic system with self-adaptive manipulation," *ACS Nano*, vol. 18, no. 14, pp. 9980–9996, 2024, pMID: 38387068. [Online]. Available: https://doi.org/10.1021/acsnano.3c11281
- [10] B. M. Pohl, A. Schumacher, and U. G. Hofmann, "Towards an automated, minimal invasive, precision craniotomy on small animals," in 2011 5th International IEEE/EMBS Conference on Neural Engineering. IEEE, apr 2011.
- [11] L. Andreoli, H. Simplício, and E. Morya, "Egg model training protocol for stereotaxic neurosurgery and microelectrode implantation," World Neurosurgery, vol. 111, pp. 243–250, 2018.
- [12] T. Okuda, K. Kataoka, and A. Kato, "Training in endoscopic endonasal transsphenoidal surgery using a skull model and eggs," *Acta neurochirur*gica, vol. 152, pp. 1801–1804, 2010.
- [13] E. Zhao, M. M. Marinho, and K. Harada, "Autonomous robotic drilling system for mice cranial window creation: An evaluation with an egg model," in 2023 IEEE/RSJ International Conference on Intelligent Robots and Systems (IROS). IEEE, 2023, pp. 4592–4599.
- [14] N. Pak, J. H. Siegle, J. P. Kinney, D. J. Denman, T. J. Blanche, and E. S. Boyden, "Closed-loop, ultraprecise, automated craniotomies," *Journal of Neurophysiology*, vol. 113, no. 10, pp. 3943–3953, jun 2015.
- [15] L. Ghanbari, M. L. Rynes, J. Hu, D. S. Schulman, G. W. Johnson, M. Laroque, G. M. Shull, and S. B. Kodandaramaiah, "Craniobot: A computer numerical controlled robot for cranial microsurgeries," *Scientific Reports*, vol. 9, no. 1, jan 2019.
- [16] D. C. Jeong, P. S. Tsai, and D. Kleinfeld, "All-optical osteotomy to create windows for transcranial imaging in mice," *Optics Express*, vol. 21, no. 20, p. 23160, Sep. 2013.
- [17] S. Hasegawa, K. Okada, and M. Inaba, "Vibration Recognition Learning System using Force and Sound Sensing integratively for Mouse Cranium Cutting in Cranial Window Surgery," in 2023 JSME Conference on Robotics and Mechatronics, Nagoya, Japan, 2023.
- [18] Y. Jia, P. M. Uriguen Eljuri, and T. Taniguchi, "A bayesian reinforcement learning method for periodic robotic control under significant uncertainty," in 2023 IEEE/RSJ International Conference on Intelligent Robots and Systems (IROS). IEEE, Oct. 2023.
- [19] Z. S. Navabi, R. Peters, B. Gulner, A. Cherkkil, E. Ko, F. Dadashi, J. O. Brien, M. Feldkamp, and S. B. Kodandaramaiah, "Computer vision-guided rapid and precise automated cranial microsurgeries in mice," *Science Advances*, vol. 11, no. 15, p. eadt9693, 2025. [Online]. Available: https://www.science.org/doi/abs/10.1126/sciadv.adt9693
- [20] N. Dvornik, K. Shmelkov, J. Mairal, and C. Schmid, "Blitznet: A real-time deep network for scene understanding," in *Proceedings of the IEEE international conference on computer vision*, 2017, pp. 4154–4162.
- [21] C.-Y. Fu, W. Liu, A. Ranga, A. Tyagi, and A. C. Berg, "Dssd: Deconvolutional single shot detector," 2017.
- [22] S. Hochreiter and J. Schmidhuber, "Long short-term memory," Neural computation, vol. 9, no. 8, pp. 1735–1780, 1997.
- [23] C. He, N. Patel, A. Ebrahimi, M. Kobilarov, and I. Iordachita, "Preliminary study of an rnn-based active interventional robotic system (airs) in retinal microsurgery," *International Journal of Computer Assisted Radiology and Surgery*, vol. 14, no. 6, pp. 945–954, Mar. 2019.
- [24] R. Li, Z. Dong, J.-M. Wu, C. J. Xue, and N. Guan, "Modeling and property analysis of the message synchronization policy in ros," in 2023 IEEE International Conference on Mobility, Operations, Services and Technologies (MOST). IEEE, May 2023.
- [25] C. Kruger, "Constrained cubic spline interpolation," Chemical Engineering Applications, vol. 1, no. 1, 2003.
- [26] S. Kumaar, Y. Lyu, F. Nex, and M. Y. Yang, "Cabinet: Efficient context aggregation network for low-latency semantic segmentation," in 2021

- IEEE International Conference on Robotics and Automation (ICRA). IEEE, May 2021, pp. 13517–13524.
- [27] C. Yu, C. Gao, J. Wang, G. Yu, C. Shen, and N. Sang, "Bisenet v2: Bilateral network with guided aggregation for real-time semantic segmentation," *International Journal of Computer Vision*, vol. 129, no. 11, pp. 3051–3068, Sep. 2021.
- [28] J. Peng, Y. Liu, S. Tang, Y. Hao, L. Chu, G. Chen, Z. Wu, Z. Chen, Z. Yu, Y. Du, Q. Dang, B. Lai, Q. Liu, X. Hu, D. Yu, and Y. Ma, "Pp-liteseg: A superior real-time semantic segmentation model," 2022.
- [29] X. Li, A. You, Z. Zhu, H. Zhao, M. Yang, K. Yang, S. Tan, and Y. Tong, Semantic Flow for Fast and Accurate Scene Parsing. Springer International Publishing, 2020, pp. 775–793.
- [30] H. Pan, Y. Hong, W. Sun, and Y. Jia, "Deep dual-resolution networks for real-time and accurate semantic segmentation of traffic scenes," *IEEE Transactions on Intelligent Transportation Systems*, vol. 24, no. 3, pp. 3448–3460, Mar. 2023.
- [31] J. Xu, Z. Xiong, and S. P. Bhattacharyya, "Pidnet: A real-time semantic segmentation network inspired by pid controllers," in *Proceedings of* the IEEE/CVF Conference on Computer Vision and Pattern Recognition (CVPR), June 2023, pp. 19529–19539.
- [32] B. V. Adorno and M. M. Marinho, "Dq robotics: A library for robot modeling and control," *IEEE Robotics & Automation Magazine*, vol. 28, no. 3, pp. 102–116, 2020.



Enduo Zhao is a postdoctoral researcher at the School of Biomedical Engineering, Tsinghua University, Beijing, China. He received a BS (2018) in mechanical engineering from Tsinghua University, Beijing, China, a MSc (2020) and a Ph.D. (2025) in mechanical engineering from the University of Tokyo, Tokyo, Japan. His research interests include automation, surgical robotics, and medical image processing.



Murilo M. Marinho (GS'13–M'18–SM'24) is a visiting researcher with the Graduate School of Medicine, the University of Tokyo, Tokyo, Japan. He is also a Lecturer in Robotics with the University of Manchester, Manchester, UK. Until late 2023, he was an Assistant Professor with the University of Tokyo. He received a BS (2012) in mechatronics engineering and a MSc (2014) in electronic systems and automation engineering from the University of Brasilia, Brasilia, Brazil, and a Ph.D. (2018) in mechanical engineering from the University of Tokyo,

Tokyo, Japan. His research interests include robotics applied to constrained workspaces and image-based automation.



Kanako Harada (M'07) Kanako Harada is a Professor at the Center for Disease Biology and Integrative Medicine (CDBIM) within the Graduate School of Medicine at The University of Tokyo, Japan. She also holds positions in the Department of Mechanical Engineering and the Department of Bioengineering within the Graduate School of Engineering. She earned her M.Sc. in Engineering from The University of Tokyo in 2001 and received her Ph.D. in Engineering from Waseda University in 2007. Before joining The University of Tokyo, she

held positions at Hitachi Ltd., the Japan Association for the Advancement of Medical Equipment, and Scuola Superiore Sant'Anna in Italy. Her research interests include surgical robotic systems, robotic automation for biomedical applications and regulatory science.